



HAL
open science

Efficient Control of a Mesoporous Fibrillar PEDOT:PSS Aerogel Structure for Promising Thermoelectric Applications

Quentin Weinbach, Swapneel Vijay Thakkar, Alain Carvalho, Gérald Chaplais, Jérôme Combet, Doru Constantin, Nicolas Stein, Dominique Collin, Laure Biniek

► To cite this version:

Quentin Weinbach, Swapneel Vijay Thakkar, Alain Carvalho, Gérald Chaplais, Jérôme Combet, et al.. Efficient Control of a Mesoporous Fibrillar PEDOT:PSS Aerogel Structure for Promising Thermoelectric Applications. *Frontiers in Electronic Materials*, 2022, 2, 10.3389/femat.2022.875856 . hal-03964088v1

HAL Id: hal-03964088

<https://hal.science/hal-03964088v1>

Submitted on 17 Nov 2022 (v1), last revised 30 Jan 2023 (v2)

HAL is a multi-disciplinary open access archive for the deposit and dissemination of scientific research documents, whether they are published or not. The documents may come from teaching and research institutions in France or abroad, or from public or private research centers.

L'archive ouverte pluridisciplinaire **HAL**, est destinée au dépôt et à la diffusion de documents scientifiques de niveau recherche, publiés ou non, émanant des établissements d'enseignement et de recherche français ou étrangers, des laboratoires publics ou privés.

Efficient control of a mesoporous fibrillar PEDOT:PSS aerogel structure for promising thermoelectric applications

Quentin Weinbach,¹ Swapneel Vijay Thakkar,¹ Alain Carvalho,¹ Gérald Chaplais,^{2, 3} Jérôme Combet,¹ Doru Constantin,¹ Nicolas Stein,⁴ Dominique Collin,¹ Laure Biniek^{1*}

¹ Université de Strasbourg, CNRS, Institut Charles Sadron UPR22, F-67000 Strasbourg, France

² Université de Haute-Alsace, CNRS, Institut de Science des Matériaux de Mulhouse (IS2M), UMR 7361, F-68100 Mulhouse, France

³ Université de Strasbourg, 67000 Strasbourg, France

⁴ Université de Lorraine, CNRS, IJL, F-57000 Metz, France

*E-mail: laure.biniek@ics-cnrs.unistra.fr

Abstract:

In this study, we describe a reproducible process route to form highly mesoporous, mechanically robust and handleable aerogels based on entangled PEDOT:PSS nanofibers. The conservation of the alcogel 3D network is ensured via thorough control of the solvent exchange and drying steps. Particular consideration has been given to metrology, allowing us to fully characterize the thermoelectric properties of the aerogels. The interconnected fibrillar morphology provides good electrical conductivity and mechanical properties by forming effective pathways for both electron transfer and sustaining mechanical forces. The Seebeck coefficient does not seem to be impacted by the high porosity of the material. Finally, the positive impact of mesoporosity on thermal transport and in particular on the lattice part of the thermal conductivity (k_{lat}) is demonstrated here for the first time. Thus, this pure PEDOT:PSS aerogel exhibits very interesting structural and charge transport properties. The high power output of $2\mu\text{W}$, measured for a temperature gradient of 36.5 K on a single aerogel sample, highlights the possibility of integrating PEDOT:PSS aerogels into thermoelectric generators.

Keywords: porous conducting polymer; mesoporous; aerogel; supercritical drying ; thermal conductivity ; charge transport properties

Introduction

Thermoelectric (TE) materials convert heat into electricity via the Seebeck effect. Utilizing these materials to produce energy from waste heat can be an interesting strategy in achieving “Net-zero” emissions. (Finn et al., 2021) The efficiency of TE materials is evaluated by the dimensionless figure of merit (zT) using the equation; $zT = \sigma S^2 T / \kappa$, where σ , S , T , κ represent the electrical conductivity ($S \cdot m^{-1}$), the Seebeck coefficient ($V \cdot K^{-1}$), the temperature (K), and the thermal conductivity ($W \cdot m^{-1} \cdot K^{-1}$), respectively. A promising choice of material for TE applications is based on the “phonon-glass electron-crystal” (PGEC) concept, i.e. where the thermal properties are similar to glass-like materials while the electrical properties are closer to those of crystalline materials. (Slack, 1995) Organic thermoelectric materials, such as doped conjugated polymers, are good candidates to achieve such properties. Indeed, their charge transport properties can be tuned by increasing the crystallinity and structural anisotropy to achieve metal-like conductivities. (Vijayakumar et al., 2019) In parallel, phonon engineering via porosity can be used to reduce the thermal conductivity. (Weinbach et al., 2021) In particular, designing the pore sizes below the mean free path of air molecules (≈ 70 nm) lowers the contribution of gas molecules to the thermal transport, while decreasing material density assists in reducing the solid material contribution to the thermal conductivity. (Tang et al., 2015; Noroozi et al., 2019) In this direction, fabricating conducting materials in the form of an aerogel (light and mesoporous material) should lead to better control on phonon engineering, which is of interest for TE application.

Aerogels are low-density bulk solids with open pores and are formed due to the interconnection of nanostructures. In general, they are fabricated from wet gels where the liquid component is replaced by air without deteriorating the porous network. (Hüsing and Schubert, 1998) This substitution is usually achieved under supercritical conditions, during which the surface tension of the supercritical fluid is negligible. Drying at this condition prevents the collapse of the pores, thereby giving the final solid a structure similar to its native gel state. (Woignier et al., 2018) Fabricating aerogels using conducting polymers offers technological advantages such as large-scale processability of a few mm-thick and very low-density solids that can be utilized to develop vertical TEG.

Conducting polymers, such as poly(3,4-ethylenedioxythiophene):poly(styrene sulfonate) (PEDOT:PSS), are of huge interest in the field of TE application due to their environmental stability, ease in doping, and commercial processability at large scales. These materials have demonstrated state-of-the-art TE performance when fabricated as films. (Bubnova et al., 2011; Kim et al., 2013) Hence, they are excellent candidates to evaluate in the form of aerogels for developing the next generation of lightweight TE devices. To date, there are very few reports on pure porous PEDOT:PSS

materials for TE applications and their fabrication methods vary by a large degree. For instance, Wang *et al* reported the fabrication of porous PEDOT:PSS by lyophilization (freezing followed by sublimation of the ice) of the commercial polymer dispersion. (Wang et al., 2019) This approach provides lightweight films after pressing the porous samples but the porosity is not defined clearly. However, interesting TE properties (power factor = $1.24 \mu\text{W}\cdot\text{m}^{-1}\cdot\text{K}^{-2}$; $\kappa= 0.1 \text{ W}\cdot\text{m}^{-1}\cdot\text{K}^{-1}$) are achieved via addition of polar solvent in the dispersion prior to freezing. In another report, Gordon *et al* developed hydrogels by rehydrating PEDOT:PSS films followed by lyophilization to remove the solvent. (Gordon et al., 2017) Here, the lyophilization highly affects the porous structure of the final product (Deville, 2017) forming macropores (50-200 μm) with no preferential orientation. After post-treatment in ethylene glycol, a power factor of $6.4 \mu\text{W}\cdot\text{m}^{-1}\cdot\text{K}^{-2}$ was obtained on such structures (it should be emphasized that no study of the effect of porosity on thermal conductivity has been conducted). Alternatively, when PEDOT:PSS gels (prepared by dropping the dispersion in ethanol) are dried in ambient conditions, dense thick films with no porosity were obtained. (Maeda et al., 2019) Nevertheless, the films displayed a high power factor of $28 \mu\text{W}\cdot\text{m}^{-1}\cdot\text{K}^{-2}$ indicating that gelation enhanced the PEDOT:PSS microstructure. In general, drying the gels by lyophilization or ambient drying techniques does not offer good control over micro/meso-porosity. In contrast, drying PEDOT:PSS alcogels (formed via the oxidative polymerization of EDOT in presence of PSS) under supercritical conditions provides highly mesoporous samples. (Zhang et al., 2010) Unfortunately, the in-situ polymerization of PEDOT led to low electrical conductivity ($0.1 \text{ S}\cdot\text{cm}^{-1}$) when compared with the samples fabricated from the commercial dispersion. Overall, controlling both the gelation of PEDOT:PSS and the drying step under supercritical conditions are the keys to maintaining sufficient charge transport properties in a well-controlled mesoporous structure.

Herein, we developed a simple and reproducible technique – to prepare mechanically robust PEDOT:PSS aerogels a few mm thick using a two-step synthesis process. The fiber-like network is created during the gelation and conserved after drying. Solvent exchanges during the gelation but also during supercritical drying are the key steps to guarantee good control over the 3D network and the porous structure. We report on the full characterization of the TE properties, including measurement of effective thermal conductivity and demonstrate the effect of porosity on the lattice part of the thermal conductivity (κ_{lat}). Altogether, the aerogels developed in this work exhibit superior TE performance as compared with other PEDOT:PSS porous systems, without any additional processing treatment (such as secondary doping or the use of crosslinker). Finally the potential use of the PEDOT:PSS aerogels in a TE generator is discussed.

Experimental Section

Materials

All materials were obtained from commercial suppliers and used as received, unless otherwise stated. PEDOT:PSS (Clevios™ PH1000, 1.0-1.2 wt.%) was purchased from Heraeus, absolute ethanol (EtOH) from Carlo ERBA, silver paste from Agar Scientific (AGG3691), liquid CO₂ and liquid ethane from Air Liquide.

Alcogel fabrication

The fabrication of the gel (called herein alcogel as it is processed in ethanol) is illustrated in Figure 1. The PEDOT:PSS polymer blend (PH1000) is received as a dispersion of nanoparticles with mean diameter of 30 nm at a weight percentage of 1.08% in water (measured on the dried dispersion). The PEDOT:PSS ratio is 1:2.5 in mass. PSS is in excess to facilitate the dispersibility of the blend in water. Based on the work of Maeda et al. (Maeda et al., 2019, 2020), the alcogels were formed by slow diffusion of ethanol (EtOH) into the PEDOT:PSS. Typically, the PH1000 dispersion was vortexed for a few minutes and then filtered through a 0.45 μm PVDF membrane to ensure homogeneous dispersion prior to use. Next, 41.5 mL of ethanol were introduced in a flat bottom Pyrex tube with an SVL screwcap. Then 5 mL of the filtered PEDOT:PSS dispersion were slowly deposited at the bottom of the vial with a syringe. Then, the mixture was immediately placed in a 90°C oil bath for 20 hours. The alcogel, while forming, took the shape of the mold (in this case, a flat bottom cylindrical tube of 22 mm inner diameter gave rise to a gel in the shape of a disc of ~17 mm diameter). The resulting sample was shrunk and floated in a transparent supernatant suggesting expulsion of liquid from the gel, also known as the syneresis effect. The supernatant was removed after gelation and the gel was washed twice with 50 mL of fresh ethanol.

Aerogel formation via supercritical CO₂ drying

Prior to drying, the upper surface of the sample was cut off (~0.5 mm thickness removal) with a razor blade to obtain a flat surface. The alcogel was loaded with a splash of EtOH into a 100 mL capacity autoclave (manufactured by SFT-110 supercritical fluid extractor) which was then sealed. The CO₂ pressure-temperature diagram is shown in Figure 1d. To ensure that CO₂ is first in the liquid phase (4°C, 750 psi in the bottle), the temperature in the autoclave was maintained at 20°C and the pressure raised to 1200 psi. The alcogel in the autoclave was stored in liquid CO₂ for 30 minutes and then the liquid CO₂ inside the autoclave was half-drained and flushed in with a fresh one. This solvent exchange was repeated five times in 30-minute intervals to completely replace EtOH with liquid CO₂

in the alcogel. After the solvent exchange was complete, the autoclave at 1200 psi was heated up to 45°C for 2 h, to induce the transition of the CO₂ from the liquid to the supercritical phase. Then, the outlet valve was slightly opened to create a dynamic flow inside the autoclave, allowing supercritical CO₂ to flow through the gel. The sample was kept under these conditions (45°C and 1200 psi) for 1 h, followed by a slow release of the pressure while keeping the temperature constant. After complete venting (approx. 30 min), the sample was transferred to a vial and degassed for a few minutes, after which the vacuum was switched to argon atmosphere for storage.

The dimensions and weight of alcogels and aerogels are measured respectively with an OTMT digital caliper and an analytical microbalance. Typically, aerogels are at least 3.5 mm thick and 1.3 cm in diameter. A consequent shrinkage from the gel to the aerogel state was observed ($\approx 40\%$ volume loss). The apparent aerogel density is very low ($\rho_{aerogel}=0.070 \pm 0.007 \text{ g.cm}^{-3}$, estimated by its mass and dimensional size) and its very high porosity Θ ($\sim 93\%$) is estimated with the following equation:

$$\Theta = \left[1 - \frac{\rho_{aerogel}}{\rho_{solid}} \right] \times 100 \quad (\text{eq.1})$$

where $\rho_{aerogel}$ and ρ_{solid} are the density of the aerogel and of PEDOT:PSS ($\rho_{solid} \sim 1.011 \text{ g.cm}^{-3}$, given by Heraeus).

Characterization methods

Scanning Electron Microscopy (SEM)

Cryo-SEM on alcogels. As ethanol is difficult to sublime, a gradual solvent exchange with deionized water was applied in the gel phase, prior to cryo-SEM analysis. The exchange was done in several incremental steps to minimize shrinkage and gel structure distortion. Typically, the alcogel (100%vol ethanol) was left for 24h in different ethanol/water (%vol) solutions (75/25, 50/50, 25/75, and finally in 100% water). Once the solvent in the gel was pure water, a small piece of gel was sliced off with a razor blade, quickly dipped into liquid ethane (used as an efficient coolant to avoid crystalline ice formation (Dubochet et al, 1988 ; Efthymiou et al, 2017)) and then transferred under high vacuum (10^{-6} mbar) and low temperature (-150°C) into the Quorum PT 3010 chamber attached to the microscope. There, the frozen sample was fractured with an adapted razor blade. After a slight sublimation of water at -90°C to reveal the details of the morphology, the sample was eventually transferred in the FEG-cryo-SEM (Hitachi SU8010) and observed at 1 kV at -150°C (under 10^{-6} mbar).

SEM: The aerogels were cut with a razor blade to reveal the surface of interest. The samples were observed at 1 kV at room temperature with the FEG-cryo-SEM (Hitachi SU8010). A high magnification image of the aerogel is also shown in Figure ES11.

X-ray Scattering

SAXS and WAXS (small- and wide-angle X-ray scattering) measurements were performed on the SWING beamline of the SOLEIL synchrotron (Saint-Aubin, France) at a beam energy of $E = 16$ keV. The sample-to-detector distance was 6.22 m and 0.52 m, respectively, covering a total scattering vector range of $0.0016 < q < 2.5 \text{ \AA}^{-1}$. The beam size was approximately $500 \times 200 \text{ \mu m}^2$ (H \times V). All measurements were performed at room temperature (22°C).

The scattered signal was recorded by an Eiger 4 M detector (Dectris Ltd., Switzerland) with pixel size 75 μm . Preliminary data treatment (angular averaging and normalization) was done using the software Foxtrot developed at the beamline, which yielded the intensity as a function of the scattering vector $I(q)$ in absolute units. Subsequent data modeling was done in Igor Pro 7.0 using functions available in the NCNR SANS package (Kline 2006) (Cylinder PolyRadius, used to model the SAXS data in Figure 2c, and Lorentzian, used to fit the WAXS peak in Figure 2d).

Nitrogen Physisorption

Textural characterization was done using a Micromeritics ASAP 2420 apparatus by determining nitrogen physisorption isotherms at 77 K. Here, the aerogel samples were cut into small pieces and loaded into an analysis tube. Prior to adsorption measurements the sample was outgassed at 423 K for 6 h under vacuum to remove the moisture from the aerogel. The specific surface area (S_{BET}) was calculated according to the criteria given in the literature (Rouquerol et al., 2007 ; Walton et al., 2007) and by using the Brunauer–Emmett–Teller (BET) method applied in the $0.02 \leq p/p^0 \leq 0.20$ ranges.

Rheology

Complex shear modulus measurements were performed with a stress-imposed rheometer (Mars III, Haake) working in oscillatory mode. For alcogel and aerogel samples, the parallel plate geometry fixtures (with different diameters) were used to cover the sample area. In the case of alcogels, the bottom plate was modified to allow the sample to be immersed in ethanol (to avoid drying during measurement). To ensure measurements in the linear response domain, the stress applied did not exceed 5 Pa. All measurements were performed at 20°C. The fixtures were adjusted according to the height of the sample without causing an excessive compression of the sample. (Collin et al., 2004) Normal force was measured simultaneously during the shear experiments.

Electrical conductivity and Seebeck coefficient

A Keithley 2634B sourcemeter and a Lab Assistant Semiprobe station inside of a Jacomex glovebox under N₂ atmosphere ($\approx 1\text{ppm O}_2$, $\approx 1\text{ppm H}_2\text{O}$) were used to measure the electrical conductivity and the Seebeck coefficient of all samples.

Electrical conductivity: The electrical resistance was measured using a standard collinear four-probe method with a probe space of 1.6 mm. The electrical resistivity and conductivity were calculated with the following equation extracted from Haldor Topsøe's geometrical factor report. (Topsøe, 1968)

$$\rho = \frac{1}{\sigma} = G \cdot \frac{V}{I}, (\text{eq. 2}) \quad \text{and} \quad G = 2\pi s \cdot T_1 \left(\frac{t}{s} \right) (\text{eq. 3})$$

where ρ is the electrical resistivity, σ the electrical conductivity, V the voltage, I the current intensity, s the probe space and $T_1 \left(\frac{t}{s} \right)$ a correctional factor for an infinite plane sample of finite thickness ($t > 2s \sim 3.2 \text{ mm}$). (Topsøe, 1968)

The experiment was performed on eight aerogels and the measurements were repeated four times on each sample.

Seebeck coefficient: To measure the Seebeck coefficient, a differential temperature method was used. A homemade setup made of one heating and one cooling Peltier cells allows an in-plane controllable temperature gradient. Measurements were performed by increasing gradually the temperature difference between the two Peltier cells up to 12.8 K (starting from 293 K, the midpoint temperature). For each temperature step, the tension was measured five times with a 20 s interval (see previous report (Hamidi-Sakr et al., 2017) for a description of the setup). To allow good thermal contact between the Peltier cells and the aerogels, copper legs (1 x 1 x 0.2 mm) were bonded on the bottom of the sample with conducting silver paste (see schematic Figure 4c). The tension was measured directly on the silver paste. Calibration of the measurement was made with a constantan wire (see supporting information for the calibration, Figure ESI4). (Bentley, 1998) The experiment was performed on six aerogels.

Cross-plane measurements: Cross plane Seebeck coefficients and output power were measured with a homemade setup, where the samples were sandwiched between hot and cold copper disks of 1 cm diameter. (Frantz et al., 2010; Danine et al., 2018) The applied pressure to the samples was below 0.3 Nm (through the use of a torque screwdriver). Using Peltier modules as heating-cooling sources and embedded thermocouples inside each copper disk, a temperature gradient was then imposed and measured across the two sides of the samples. An external cooling flow system, with the help of a

cryostat, was used to keep the thermal gradient across the sample thickness. The operating temperature was defined as 293 K, whereas the maximal thermal gradient was fixed to 7 K. The system allows measuring the potential difference ΔU and the temperature difference ΔT , giving the Seebeck coefficient α from the slope $\Delta U/\Delta T$ of the voltage-temperature curve. Considering the sample as a thermoelectric generator, the output power was determined as a function of an adjustable external load circuit. When the output power is at its maximum, the load resistance is then equal to the internal resistance of the sample.

Thermal conductivity

The thermal conductivity of the aerogels was measured using the transient plane source (TPS) technique by utilizing a commercial apparatus (Hot Disk®, TPS 1000). Here, the sensor of radius 3.189 mm (composed of a Nickel double spiral protected with a thin layer of Kapton insulator) was sandwiched between two PEDOT:PSS aerogels, as illustrated in Figure 4e. Only samples with appropriate dimensions in regards to the sensor radius can be considered to satisfy the heat conductivity equation in a thermally infinite medium. The distance from the sensor edge to the nearest free boundary of the sample should be at least equal to the sensor radius (i.e. with this sensor, only samples of minimum 12.8 mm in diameter and 3.2 mm in thickness can be treated).

The setup was placed under a metallic bell to avoid any temperature fluctuations arising from air currents. Before each measurement, the sample was degassed for 30 minutes to remove the adsorbed moisture from the aerogels and stabilized at room temperature for 10 min to avoid temperature drift of the sample. The thermal equilibrium of the sample was also checked for 40 s before each measurement. The room temperature (in general 19-21 °C) was recorded using a thermocouple, and the value was incorporated in the software prior to launching the measurement.

During the measurement, an electrical current of known power and duration is passed through the sensor which also records the increase in temperature of the sensor as a function of time. The temperature increase ($\overline{\Delta T}$) across the sensor area is measured by monitoring the total resistance of the sensor according to the following equation:

$$R(t) = R_0 + [1 + \alpha \overline{\Delta T}(\tau)] \text{ (eq. 4)}$$

where R is the total electrical resistance at time t , R_0 is the initial resistance at $t = 0$, $\alpha = 6.41 \times 10^{-3} \text{ 1/}^\circ\text{C}$ is the temperature coefficient of resistivity of nickel. Therefore Eq. 4 allows us to accurately determine $\overline{\Delta T}$ as a function of time, which is actually recorded by the TPS1000 analyzer (a typical transient curve is given in Figure 4f). In general, 200 experimental points are obtained from this graph and the first 15 data points from this curve are eliminated prior to calculation - as they are also

affected by the resistance of the air layer between sensor and sample. The optimal time window (i.e. the data point interval to consider) was selected to meet the best conditions to be within the limits of total characteristic time. (Bohac et al., 2000) Plotting the temperature increase on a $t^{-1/2}$ scale and locating on the more linear part of the curve corresponds to the plot $\overline{\Delta T}$ as a function of $D(\tau)$. A straight line should be obtained (a typical curve is shown in Figure 4g). According to equation 5, the thermal conductivity κ , can be calculated from the slope of that line:

$$\overline{\Delta T}(\tau) = \frac{P_0}{\sqrt{\pi^3} r \kappa} D(\tau) \text{ (eq. 5)}$$

With P_0 , the total output of power from the sensor during the transient, r , the radius of the largest ring of the sensor, $D(\tau)$ a complex dimensionless time dependent function (with $\tau = \sqrt{\frac{t}{TCR}}$, t the time measured from the start of the transient recording and TCR, the total characteristic time). (Bohac et al., 2000)

The output power and duration time required for a reliable measurement depends strongly on the characteristics of the sample. We first used the reported conditions for polyurethane foams (a thermally isolating lightweight sample with a known $\kappa = 0.042 \text{ W}\cdot\text{m}^{-1}\cdot\text{K}^{-1}$) measurements and then a trial-and-error approach to reach the best conditions to be within the limits of total characteristic time (between 0.33 and 1), (Bohac et al., 2000) temperature increase ($2 < \Delta T < 5\text{K}$) and penetration depth (larger than $\sqrt{4\alpha t}$ with α , the thermal diffusivity of the sample and t the measurement time). (He, 2005) Evaluation of the results was also done by assessing the residual curve (Figure ESI6), which represents the temperature difference between the theoretical Hot Disk model and the experimental data. In the ideal case, the residuals should be randomly scattered around a horizontal line. The experiments were performed in ambient conditions and the input power and time duration were set at 10 mW and 10 s, respectively. The experiment was performed on six aerogels and the measurements were repeated several times.

Results

PEDOT:PSS aerogel fabrication

The fabrication of PEDOT:PSS aerogels involved two fundamental steps: (i) gelation step, followed by (ii) drying of gels under supercritical conditions.

To ensure the formation of a robust 3D network, a PEDOT:PSS gel was formed prior to drying. Different ways are described in the literature to produce PEDOT:PSS gels: herein, we followed the

work of Maeda and co-workers. (Maeda et al., 2019, 2020) Typically, the PEDOT:PSS aqueous dispersion is poured at the bottom of a vial filled with ethanol. Due to the density difference between the two liquids, the dispersion remains at the bottom of the vial (as shown in Figure 1 a). Upon time and at high temperature, ethanol diffuses slowly into the PEDOT:PSS dispersion. A bluish layer appears at the interface of the two phases (Figure 1 b) which highlights the solvent exchange process. After 20 h, a solid and dark blue alcogel floating in a transparent solution is obtained and the supernatant is replaced with fresh ethanol (Figure 1c). This gelation process results in a handleable alcogel whose size and shape can be tuned by using a different mold or cutting it accordingly.

The gelation mechanism is still under investigation. Maeda et al. suggested that excess PSS was removed upon the interaction of the dispersion with ethanol, forming gradually a gel state from the surface to the interior. (Maeda et al., 2019) Our investigation using cryo-SEM (discussed below), shows that the initial micelle-like structure of PEDOT:PSS dispersion (as usually described in the literature) converts into the fibrillar structure during this gelation mechanism.

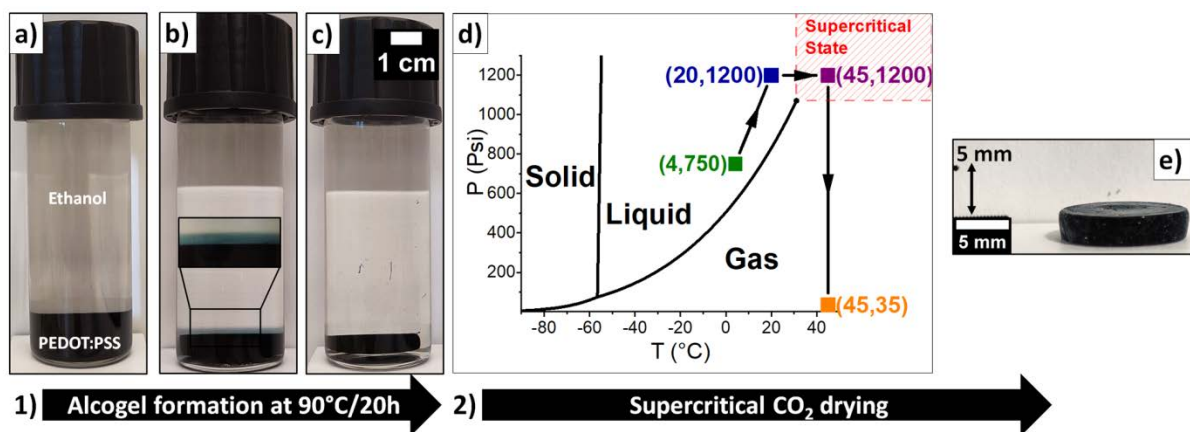


Figure 1: Two-step PEDOT:PSS aerogel formation process. a-c) Photographs were taken during the gelation process at different times: a) $t = 0$, PEDOT:PSS is deposited at the bottom of ethanol, b) $t = 10$ h, interaction between ethanol and PEDOT:PSS is visible at the interface of the two phases, c) $t = 20$ h, the alcogel is formed. d-e) Supercritical drying process: d) schematic of supercritical drying steps in the (P,T) CO₂ diagram; in green: initial temperature and pressure in the closed autoclave containing the alcogel sample, in blue: ethanol-CO_{2,Liquid} exchange, in purple: supercritical state of CO₂ and dynamic drying, in orange: venting step, e) Resulting PEDOT:PSS aerogel.

Next, the PEDOT:PSS alcogels were subjected to supercritical drying, providing aerogels. The conditions of this drying are critical to minimize shrinkage and possible gel distortion. Since the gel produced after the synthesis contained EtOH in its pores, the solvent was first replaced with liquid CO₂ to facilitate the supercritical drying at mild conditions. The replacement was achieved by a solvent exchange process in the autoclave, during which the concentration of EtOH in the pores decreases due to its miscibility with liquid CO₂ and the diffusion of liquid CO₂ in the gel under high-pressure conditions (Figure 1d, in blue). After the solvent exchange was completed, the autoclave

was heated until the conditions reached beyond the supercritical point of the liquid CO₂ (31 °C, 1070 psi, see Figure 1d, in purple). During the heating, the surface energy associated with the liquid-gas interface diminishes, which results in the transformation of the liquid CO₂ present in the pores to a supercritical fluid. The capillary forces acting on the network are null, and extracting the fluid from the sample in this condition results in the conservation of the network structure. Therefore, venting (Figure 1d, purple) the autoclave at this condition prevents the collapse of the gel. The resulting aerogel monolith (Figure 1e) is crack-free and retained the same features of the alcogel. However, in our case it suffered from a 40%vol shrinkage which might be attributed to the interaction of the alcogel with liquid CO₂ during the solvent exchange process, as this behavior is also seen for PEDOT:PSS gels when immersed in other solvents. Despite optimizing the solvent exchange process, the shrinkage could not be avoided. Nevertheless, the final sample size is still large enough (thickness: 3.5 mm, diameter: 13 mm) to allow the accurate mechanical and thermoelectric characterizations. The aerogels exhibit ultra-low density of 0.07 g.cm⁻³ with porosity of 93 %.

Morphology of the mesoporous alcogel and aerogel

Cryo-SEM was performed on the alcogel to observe its native network. First, the gel solvent (ethanol) was replaced by water via several washes (see details in the experimental section). Then, the gel was frozen very quickly in a liquid ethane slush for a few minutes. As the freezing rate is extremely high, the water does not have time to crystallize. Thus, the amorphous ice formed preserves the original structure of the gel. The frozen gel is placed into the cryo-SEM chamber where it is cut with a razor blade to reveal its structure. It is finally sublimated to remove a thin layer of ice. The structure, presented in Figure 2a, is composed of PEDOT: PSS fibers of 11 ± 2 nm mean diameter. They are well interconnected and form a nanostructured 3D network. The aerogel was observed by SEM and its mesoporous structure is presented in Figure 2b. The network is similar to that of the wet gel which is composed of entangled fibers of 9 ± 2 nm mean diameter. The sizes of the voids are estimated within the 10-50 nm range. The textural properties were also confirmed by nitrogen adsorption /desorption tests (see Figure ESI1). A type IV isotherm with adsorption hysteresis at high relative pressure indicates a large number of mesopores formed due to the interconnection of the fibers. A trace amount of macropores, not detectable by nitrogen physisorption might be present in the sample. A very small percentage of micropores can be assessed. The large BET surface area of 315 m² g⁻¹ can be correlated to an apparent external surface due to the fibrillar nature of the objects.

X-ray scattering experiments were performed at synchrotron Soleil. The scattering of nanostructure constituting the aerogel was studied with the small angle module (SAXS), whereas the polymer chains packing within the nanostructures was analyzed by wide-angle X-ray scattering experiments

(WAXS), (Figure 2c-d). At small angles ($0.002 \text{ \AA}^{-1} < q < 0.03 \text{ \AA}^{-1}$), the intensity profile decreases and follows a q^{-1} power law (Figure 2c). This dependence highlights the one dimensionality of the observed nano-objects composing the aerogel. The SAXS domain can be fitted with a cylinder model (of infinite length) with radius polydispersity (Figure 2c inset), yielding a diameter distribution in the range of 3 to 8 nm. This finding correlates well with the fibrillar structure of the aerogel observed in SEM. At wide angles ($0.3 \text{ \AA}^{-1} < q < 2.5 \text{ \AA}^{-1}$), a series of scattering peaks related to the inner structure of the fibers, can be observed (Figure 2d). Five peaks at q values of 0.49, 0.71, 0.98, 1.23 and 1.85 \AA^{-1} correspond to lattice spacing of 12.8, 8.8, 6.4, 5.1 and 3.4 \AA , respectively, according to Bragg's law. A consensus the assignment of PEDOT:PSS X-ray diffraction peaks has not yet been reached in the literature. Some structural models propose that the spacings at 12.8 \AA and 5.1 \AA are related to the packing distance of PSS chains. The attribution of the two other peaks (8.8 and 6.4 \AA) is not yet clearly understood. (Kim et al., 2012; Takano et al., 2012; Massonnet et al., 2014) Another structural model by Hosseini et al, (Hosseini et al., 2020) attributes the peak at 12.8 \AA to the second order of interlamellar spacing between two side-by-side PEDOT lamellae. In all cases, the well-defined peak at small distance (3.4 \AA) is known to be the characteristic of the π - π stacking distance of the PEDOT aromatic rings. Interestingly, the π - π stacking spacing measured in the aerogel is slightly lower than the one measured on non-treated PEDOT:PSS films (3.5 - 3.6 \AA) suggesting some increase in molecular packing degree. (Kim et al., 2012) The structural order of PEDOT within the fibers was investigated by fitting the peak at 1.85 \AA^{-1} with a Lorentzian model: $I(q) = \frac{I_{\max}}{1 + \left(\frac{q - q_0}{\gamma}\right)^2}$. The half-width at half maximum (HWHM) of the peak, γ , is related to the domain size D by the Scherrer equation: $D \cong \frac{2\pi}{\gamma}$. This relation is equivalent to the more common form $\cong \frac{K\lambda}{B \cos \theta'}$, where we assume the Scherrer constant $K = 1$ for coherence with the existing literature. (Takano et al., 2012) Fitting directly the $I(q)$ data (red line in Figure 2d) yields $D = 5.5 \text{ nm}$, but the fit is not very good, since the experimental peak is asymmetric. A better fit is obtained by using the Kratky plot $q^2 I(q)$ as a function of q and yields $D = 6.8 \text{ nm}$ (see Figure ESI2). Therefore, the size of the PEDOT crystallite domains along the π - π stacking direction (along the b-axis) reaches 6.8 nm , corresponding to ~ 19 - 20 stacks of PEDOT oligomers. As a comparison, pristine PEDOT:PSS films or films treated with ethylene glycol present lower crystallite size of $D \sim 1.2 \text{ nm}$ and $D \sim 4.5 \text{ nm}$, respectively. (Takano et al., 2012) Although we cannot conclude on the orientation of the stacks within the fiber, it is worth noticing that the domain size along the π - π stacking direction of PEDOT is comparable to the diameter of the fiber. Altogether, the WAXS experiment highlights the great degree of order of PEDOT chains induced by the gelation process which is conserved after drying.

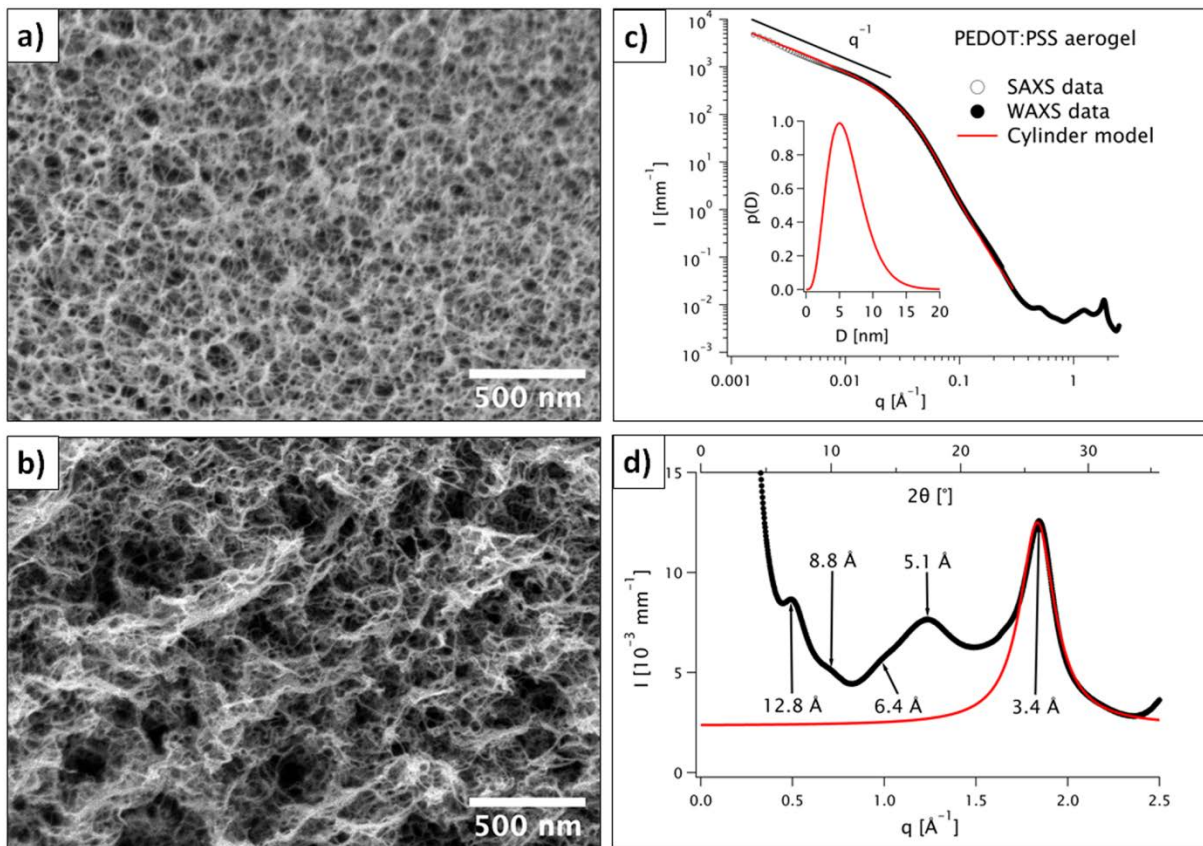


Figure 2: a) Cryo-SEM image of the alcogel, b) SEM image of the aerogel, c) Scattered intensity as a function of the scattering vector, $I(q)$, for the SAXS and WAXS configurations (open and solid dots, respectively) and fit with a cylinder model (the diameter polydispersity is described by a Schulz distribution $p(D)$, displayed in the inset). The low- q power law $I(q) \sim q^{-1}$ is shown above the data. d) WAXS signal $I(q)$ (solid dots). The abscissa is also given as 2ϑ for Cu $K\alpha$ radiation along the top axis. The peaks are identified by arrows and labeled with the corresponding distances. The Lorentzian fit of the 3.4 Å peak is shown as a red solid line.

Mechanical properties

The mechanical properties of both alcogels and aerogels have been investigated by steady state rheology. Figure 3a shows the typical response of the alcogels under oscillatory shear. It is characterized by a quasi-constant behavior of the storage modulus G' and of the loss modulus G'' with frequency. From the G' -plateau value, an elastic shear modulus of ~ 10 kPa can be deduced. This value is a hundred times higher than other PEDOT:PSS gels modulus reported in the literature. (Yao et al., 2017; Feig et al., 2018) To ensure reproducibility, several alcogels were examined: the measurements led to the same qualitative behavior and values of G' close to 10^4 Pa. Moreover, to verify the homogeneity of the alcogels, the mechanical response of three horizontal sections of the same sample (located on the upper, middle, and lower part of the sample, respectively) were examined (Figure ESI 3A). The results obtained show almost identical values with no particular trend.

Therefore, from a macroscopic point of view, alcogel samples are homogeneous and do not show any mechanical anisotropy. Thus, the gelation seems to be isotropic and homogeneous in the conditions of preparation (with no gradient of polymer chain concentration in the sample linked to a flocculation/sedimentation effect during gelation). Furthermore, the G' and G'' behaviors at low-frequency (Figure 3a) are characteristic of the rheological response under shear as expected for a physical gel in the hydrodynamic regime. This behavior is also consistent with the low-frequency response of a chemical gel with a large number of inhomogeneities. (Rubinstein and Colby, 2003) To distinguish between chemical bonding and physical binding constituting the alcogel network, a static compression can be applied to the material, followed by examination of the evolution of the normal reaction force of the sample. Depending on the nature of the nodes forming the network, this normal force will be maintained over time in the case of permanent nodes (chemical gel) or will relax over time if the nodes are transient (physical gel). The inset of Figure 3b focuses on the short times and shows simultaneously the increase in normal force and the progressive decrease in sample thickness (9% in our case over 1 min of contraction time). A rapid increase in normal force during sample compression, followed by a gradual decrease in this force over time is observed (Figure 3b). This highlights that the alcogel reacts like a physical gel (as also observed for PEDOT:PSS hydrogel (Yao et al., 2017)) since it relaxes its force over time. At the end of the experiment, while the upper plate of the cell returned to its pre-compression position, the sample did not return to its initial thickness, indicating that the change in size was irreversible. Figure 3b also shows two regimes of force decay with time: a rapid decay that extends up to ~ 5 h, followed by a slower decay that extends to the end of the experiment (described by a simple linear decrease with time). Assuming that this linear decrease is maintained over time, this force vanishes after 57 h. In other words, we can identify this time with the lifetime of the longest relaxation mode of the alcogel lattice (demonstrating that some elasticity endures over time).

To allow a quantitative comparison of the mechanical properties prior to and after drying, the same sample was studied, first in its alcogel state and then in its aerogel state. Figure 3c shows the typical frequency response of the aerogel. This response is qualitatively very similar to that of alcogel, with in particular the existence of a low-frequency plateau for G' and G'' . A slight difference is observed for the plateau of G'' , which persists at higher frequencies for aerogel than for alcogel. This frequency extension of the plateau reflects the increase in the lowest relaxation frequency of the internal lattice modes. Approximately a factor of two in the increase in elastic modulus between the alcogel and the aerogel was observed. As shown previously (Figure 1), supercritical drying also leads to a reduction in sample size. Within the accuracy of the measurements, the volume change and the modulus change induced by supercritical drying are comparable ($V_{\text{aerogel}}/V_{\text{alcogel}} = 0.59$ with $V_{\text{alcogel}} = 0.835 \text{ cm}^3$ and $V_{\text{aerogel}} = 0.489 \text{ cm}^3$ and $G'_{\text{alcogel}}/G'_{\text{aerogel}} = 0.61$, see Supporting Information Figure

ESI3b). Since the elastic moduli are proportional to the node density of the network, the number of nodes in the alcogel network remains the same after supercritical drying. The initial network in the alcogel is thus preserved during the aerogel formation.

In summary, the results of the rheology experiments on alcogels show the expected behavior for a physical gel: stress relaxation and frequency response characterized by a low-frequency G' - and G'' -plateau. The formulation of alcogels yields samples which are isotropic and homogeneous at the macroscopic scale, and whose elastic modulus is around 10 kPa. The aerogel shows a similar rheological behavior as the alcogel, but with twice the elastic modulus (~ 20 kPa). A precise analysis of the results carried out on the same sample in the alcogel and aerogel states shows that the increase in elastic modulus comes from the reduction in the volume of the sample during supercritical drying, while the number of nodes for alcogel and aerogel remains the same. Altogether, the aerogels show interesting structural features that sound promising for TE application.

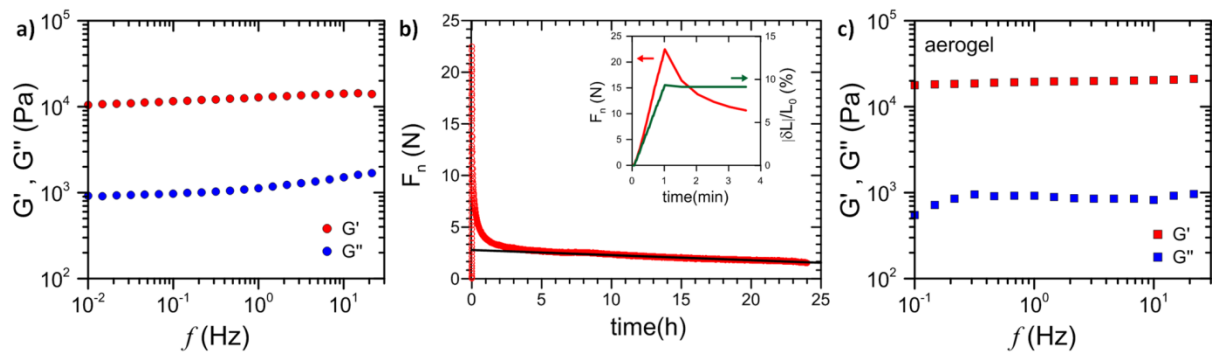


Figure 3: a) Complex shear modulus variation with frequency for an alcogel sample, b) evolution over time of the normal force of an alcogel sample subjected to a reduction in thickness. The time relaxation of this force highlights the physical gel nature of the alcogel, c) complex shear modulus variation with frequency for an aerogel sample.

Thermoelectric properties

Electrical resistance, Seebeck coefficient and thermal conductivity were measured on each sample to ensure a clear correlation between all TE properties. Six to eight different samples were in total to guarantee accurate reproducibility of the results. As a non-destructive method, thermal conductivity was first measured, then electrical resistance before the Seebeck coefficient that required the use of silver paste for a better electrical contact (for the 'in-plane' method). Figure 4 shows how the samples have been characterized and a representative curve for each of the measurements. The method of sample preparation for these TE characterizations is described in the experimental section.

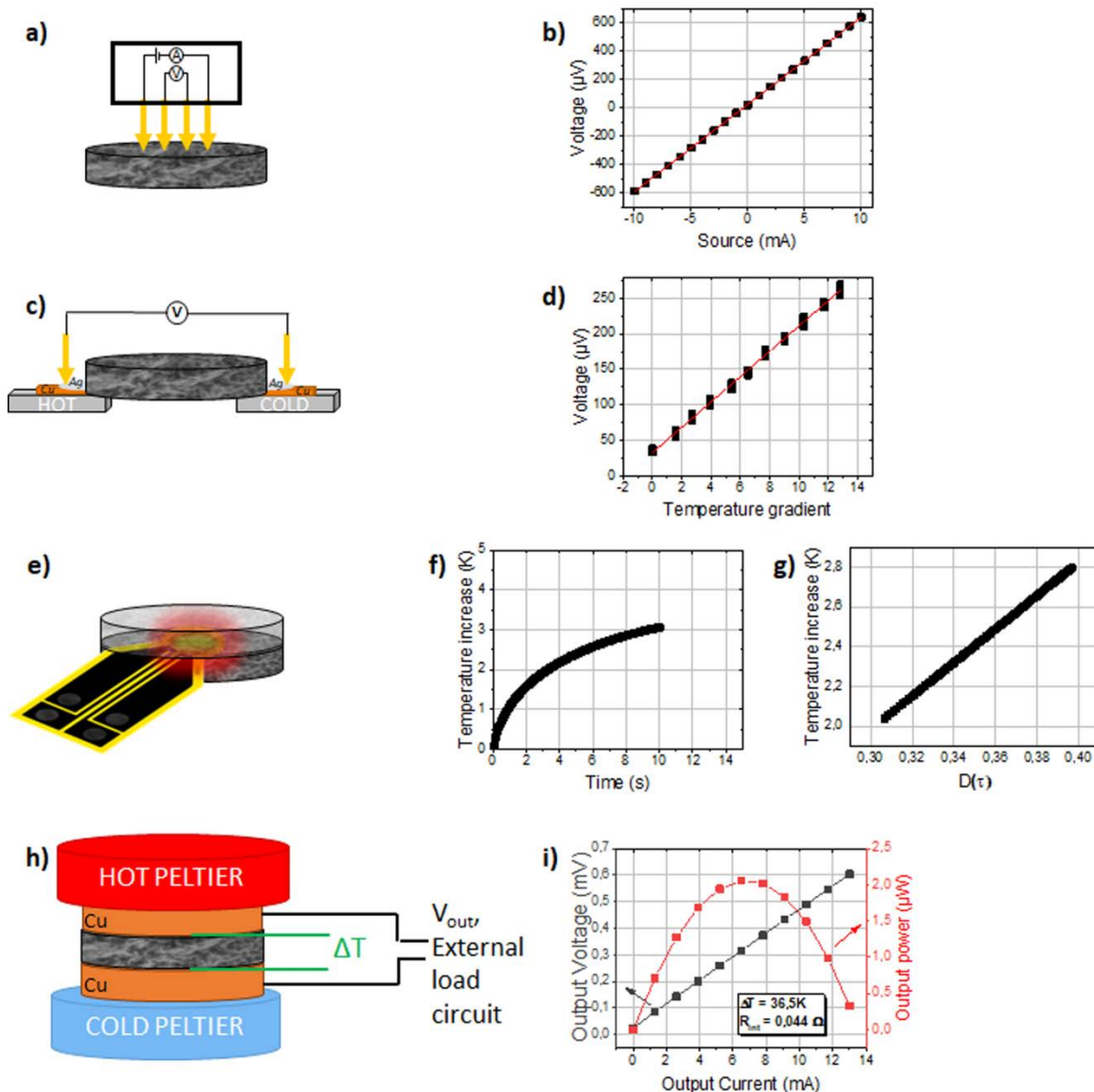


Figure 4: a) Schematic of the electrical resistance measurement using the four-point probe geometry on the aerogel, b) typical I/V curve of the electrical resistance measurement, c) schematic of in-plane Seebeck coefficient measurement. To ensure good electrical contact with the probes and a good thermal contact with the Peltier elements, aerogel samples have been pasted on copper foil (Cu) with silver paste (Ag), d) typical curve for Seebeck measurement, e) sample configuration for isotropic thermal conductivity measurement, the sensor is sandwiched between two aerogels of fairly identical size. The samples were held in place using a lightweight aluminum pellet at the top of the upper sample, which ensured good contact between the sensor and the surface of the samples, f) typical transient curve of thermal conductivity measurements, g) Typical calculated graph (ΔT) as a function of $D(\tau)$, h) schematic of cross-plane Seebeck coefficient and power output measurements, i) output voltage and output power as a function of current for a typical aerogel for a temperature gradient of 36.5 K.

Electrical resistance was measured on the aerogels with a four-probe collinear resistivity setup (as shown in Figure 4a). The resistance appears to be isotropic (measured on both sides of eight samples, on different spots). A typical I-V curve is presented in Figure 4b). The aerogels display a mean electrical conductivity value of $18.1 \pm 1.0 \text{ S}\cdot\text{cm}^{-1}$ which is amongst the highest values reported

for pure and porous PEDOT:PSS materials with such high thickness and low density (see Table 1 for comparison). We suggest that such high charge transport property in a highly porous material is due to the long-range nanostructuring of the polymer chains within the fibers during the gelation step (see the WAXS discussion above on the coherence length of the PEDOT domains along the π - π stacking direction). Furthermore, the interconnected fibrillar morphology provides good electrical conductivity by forming effective pathways for electron transfer.

To evaluate the electrical conductivity of our highly porous PEDOT:PSS aerogels (93% porosity) as compared with solid PEDOT:PSS films (no porosity), we can follow different approaches. Experimentally, we have dried the PEDOT:PSS alcogels in air which afforded inhomogeneous but self-supported thick films ($\sim 10 \mu\text{m}$) displaying an electrical conductivity of $403 \pm 53 \text{ S.cm}^{-1}$. This value is close to the ones reported by Maeda and co-workers (Maeda et al., 2019). Theoretically, we can also consider mathematical models that take into account the pore geometry and the volume fraction of the pores to determine the electrical conductivity of the solid without pores (i.e., σ_0). However, these models have been mostly developed for closed-cell metallic foams, which are far from the structure reported in this work. (Liu et al., 1999; Dharmasena and Wadley, 2002; Goodall et al., 2006; Cuevas et al., 2009) Interestingly, the model developed by Ashby et al. describes a general equation for open-cell porous materials. (Ashby et al., 2000) In this model, the cell edges form a 3D network in which one-third of the cell edges are aligned with the potential gradient. This model also takes into account the contribution of nodes in the electrical path. Although this model is only strictly applicable in an ideal system, we chose to use it here because the aerogel shows an open cell structure with a large number of nodes (see SEM and rheology). Accordingly, σ_0 of the solid PEDOT:PSS material can be estimated at around 507 S.cm^{-1} using the following equation (Ashby et al., 2000):

$$\sigma_0 = \frac{\sigma_{porous}}{\frac{1}{3}[(1 - \Theta) + 2(1 - \Theta)^{\frac{3}{2}}]}$$

where σ_{porous} is the apparent electrical conductivity measured on the porous material, and Θ the porosity of the material. The value obtained here is in fair agreement with the experimental data ($403 \pm 53 \text{ S.cm}^{-1}$). Optimizing the theoretical model is out of the scope of this manuscript but Ashby's model could be considered for fibrillar porous structure. Most importantly σ_{porous} values of the aerogels ($\sim 18 \text{ S.cm}^{-1}$) are higher than the other reports on porous PEDOT:PSS (prior post-treatments, see Table 1). This enhancement can be attributed to the good structuring of the polymer chain within the fibers during the gelation step.

The Seebeck coefficient S was measured in-plane on six samples via the differential method (see Figure 4c). The value is calculated by linearly fitting a series of measured thermovoltages over a series of temperature differences across the sample ($S = -\frac{dV}{dT}$) (a typical curve is shown in Figure 4d). This p-type material exhibits a positive Seebeck coefficient of $18 \pm 1 \mu\text{V.K}^{-1}$. Additionally, the Seebeck coefficient was also measured in a cross-plane configuration (see Figure ESI 5a) with a $\Delta T_{\text{max}} = 6 \text{ K}$, centered around 293 K. Both in-plane and cross-plane values are consistent, which confirms the structural isotropy of the sample and the appropriate metrology used to characterize bulk samples. These results also correlate with values reported in the literature for PEDOT:PSS dense films swollen in ethanol ($S = 18 \mu\text{V.K}^{-1}$). (Maeda et al., 2019) It is worth mentioning that the Seebeck coefficient was not impacted by the high porosity of aerogels (high air content), as also observed in the case of P3HT foams. (Kroon et al., 2017)

Thermal conductivity was measured using the transient plane source method (Hot Disk TPS1000 analyzer). The standard uncertainty for thermal conductivity values is given at 5%. The technique provides nondestructive and rapid measurements of both thermal conductivity and diffusivity. The method principle is described in the experimental section.

The measurements were performed on three pairs of aerogels and repeated consecutively ten times with an interval of 30 min between each trial. The average thermal conductivity of the aerogels was calculated to be $0.065 \text{ W.m}^{-1}\text{.K}^{-1}$ (thermal diffusivity = $0.55 \text{ mm}^2\text{.s}^{-1}$). This low value accounts for the high porosity of the aerogels and their mesoporous structure. Considering the Wiedemann-Franz law (with a Lorenz number close to the Sommerfeld value (Sommerfeld, 1927)) and the electrical conductivity of our aerogel, we estimate $\kappa_{\text{elec}} = 0.013 \text{ W.m}^{-1}\text{.K}^{-1}$ and $\kappa_{\text{lat}} = 0.052 \text{ W.m}^{-1}\text{.K}^{-1}$ at room temperature. It is typically assumed that the κ_{lat} of TE conducting polymer (in film) is $0.2 \text{ W.m}^{-1}\text{.K}^{-1}$. (Dongmin Kang and Jeffrey Snyder, 2017) Furthermore, a substantial decrease of $\kappa_{\text{lat}} (< 0.2 \text{ W.m}^{-1}\text{.K}^{-1})$, can help to attain $zT > 1$ for organic thermoelectrics (if the energetic disorder is also minimized). (Scheunemann and Kemerink, 2020) In this work, we demonstrate that introducing porosity and phonon engineering of conducting polymers is an efficient strategy to decrease κ_{lat} by a factor of 4.

Finally, from the thermoelectric properties obtained above, a zT of 2.7×10^{-3} at 300 K was calculated for mesoporous PEDOT:PSS aerogels. This value is highest amongst those reported in the literature for such thick and light-weight samples. Table 1 summarizes the properties of the PEDOT:PSS aerogels of this work in relation with the existing literature. An exact comparison with other reported values is difficult as porous PEDOT:PSS materials are processed differently which impacts their structural and functional properties. As discussed earlier, most of the reports either omit the gelation aspect of the synthesis or utilize different drying techniques to obtain porous solids (comprised of

macropores). To compensate for the resulting poor TE features, they utilize post-processing steps such as immersing in organic solvents (Gordon et al., 2017; Yanagishima et al., 2020) or compression (Wang et al., 2019). However, this comes at the cost of sample shrinkage (pore collapse) or of decrease in sample size (increase in density) respectively. Furthermore, the structural and textural features were not studied in detail and the functional properties were not characterized extensively.

To demonstrate the high potential of these samples in a TE generator, the power output was measured as a function of an adjustable external load circuit in air (at ambient temperature). Here, an aerogel was sandwiched between two copper discs and a temperature gradient of 7 K was applied through two Peltier elements (see Figure 4.h). The maximum power output is determined when the load resistance is equal to the internal resistance of the sample (see Figure 4.i). The aerogel exhibits a maximum power output of 0.102 μW and a small internal resistance of 0.037 Ω for a small temperature gradient of 7 K (Figure ESI5b). Interestingly, the maximum power output is increased twenty times to 2 μW for a temperature gradient of 36.5 K. The evolution of power output as a function of temperature gradient follows a 2nd order polynomial function (Figure ESI 5c). This measurement demonstrates the power output of a one-leg thermoelectric generator. Increasing the number of legs and coupling with n-type aerogel counterparts (with balanced properties) can lead to promising next-generation TE generators. For instance, Wang et al (Wang et al., 2019) developed a TE generator consisting of six pairs of p-type PEDOT:PSS-based cryogel (with heterogeneous macroporosity) and n-type CNT fibers as legs and the maximum power output of 0.62 μW was generated at a temperature gradient of 60 K.

Table 1: Physical and TE measured properties of the PEDOT:PSS aerogel fabricated herein compared with other porous PEDOT:PSS and P3HT reported in the literature with t , the thickness, ρ , the density, and BET surface extracted from the Brunauer- Emmett – Teller method. NCF stands for nanofibrillated cellulose and GOPS for glycidoxypropyl trimethoxy silane.

REF	Condi tions	t (mm)	ρ ($\text{g}\cdot\text{cm}^{-3}$)	Porosity (%)	BET		σ ($\text{S}\cdot\text{cm}^{-1}$)	S ($\mu\text{V}\cdot\text{K}^{-1}$)	κ_1 ($\text{W}\cdot\text{m}^{-1}\cdot\text{K}^{-1}$)	zT ($\times 10^{-3}$) @300K
					surface area ($\text{m}^2\cdot\text{g}^{-1}$)	Pore size				
This work	As obtained porous PEDOT:P SS	3.4 ± 0.2	$0.070 \pm$ 0.007	93	315	20-50 nm	$18.1 \pm$ 1.0	18 ± 1	0.065 ± 0.003	2.7 ± 0.2
(Zhang et al.,	As obtained	/	0.138- 0.232	/	227	12-16 nm	$\sim 10^{-1}$	/	/	/

2010)	porous PEDOT:P SS										
(Yanagis hima et al., 2020)	Porous PEDOT:P SS after dipping for 1h in methanol	0.99	0.108	91	/	macro	7.9	20.3	0.04 (estimated)	2.4 (estimated)	
(Wang et al., 2019)	Porous PEDOT:P SS containin g 5%vol NMP and compress ed	0.11	0.25	Compressed porous film		macro	35	18.8	0.10	3.7	
(Gordon et al, 2016)	As obtained porous PEDOT:P SS	~ 0.5	/	/	/	macro	< 1	~ 18	/	/	
(Khan et al, 2016)	Porous PEDOT:P SS containin g NCF and GOPS	~ 2-3	/	/	/	macro	0.001	37	/	/	
(Kroon et al, 2017)	F4TCNQ doped - P3HT foam	4		66		Macro pores and mesop ores	0.22	68.4	0.14	0.23	

Conclusion

Here, we have developed a facile process to prepare aerogels that display values competitive with the literature without any post-processing techniques. Moreover, we have established an in-depth study on the aerogels using state-of-the-art characterization tools. We demonstrate the production of homogeneous PEDOT:PSS physical gels over a few mm thickness with high reproducibility. Their fibrillar 3D network is evidenced by SEM images and confirmed by X-ray scattering measurements. Moreover, as demonstrated by rheological studies, the strong network is homogeneous throughout the sample. It is demonstrated by SEM images and modulus measurements that the 3D mesoporous

network is conserved in the dried state, despite 40% of the volume loss after drying. The final aerogels are ultralight, handleable, and mechanically robust. With respect to the functional properties, the electronic charge transport was studied thoroughly correlating experimental and theoretical models. A sufficient electrical conductivity was maintained through nanostructuration and the thermal conductivity was reduced due to phonon engineering. Altogether, the combination of both strategies produces a high power output of p-type one-leg-TEG, the next step being the development of its n-type counterpart.

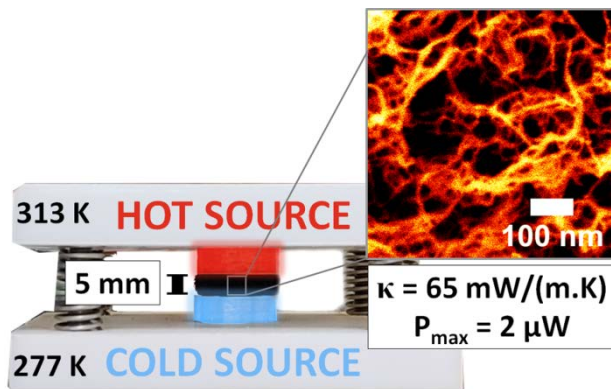
Acknowledgments

Financial support by ANR JCJC 2019 (BODYTEG) and Région Grand Est 2020 are gratefully acknowledged. Thermoconcept (Cynthia Besson and Alexandre Renault) is acknowledged for training and technical support on the TPS1000 machine. The PLAMICS microscopy facility of ICS is acknowledged for technical support and the use of their equipment. We acknowledge SOLEIL for provision of synchrotron radiation facilities and we thank Thomas Bizien for assistance in using beamline SWING for the SAXS and WAXS experiments. Martin Brinkmann is acknowledged for providing access to the Seebeck in-plane measurement set-up and the collinear four-probe setup both located in a glove box. Patrick Allgayer, Laurent Hermann and Jean-Philippe Lamps are thanked for technical support. We acknowledge Marc Schmutz and Duncan Schwaller for fruitful discussions.

Conflict of interest

There are no conflicts to declare.

Graphical abstract



References

- Ashby, M. F., Evans, A. G., Fleck, N. ., Gibson, L. J., Hutchinson, J. ., and Wadley, H. N. G. (2000). *Metal Foams : a Design Guide*. Boston: Butterworth-Heineman.
- Bentley, R. E. (1998). *Handbook of Temperature Measurement Vol. 3: The Theory and Practice of Thermoelectric Thermometry*. Singapore: Springer Science & Business Media.
- Bohac, V., Gustavsson, M. K., Kubicar, L., and Gustafsson, S. E. (2000). Parameter estimations for measurements of thermal transport properties with the hot disk thermal constants analyzer. *Rev. Sci. Instrum.* 71, 2452–2455. doi:10.1063/1.1150635.
- Bubnova, O., Khan, Z. U., Malti, A., Braun, S., Fahlman, M., Berggren, M., et al. (2011). Optimization of the thermoelectric figure of merit in the conducting polymer poly(3,4-ethylenedioxythiophene). *Nat. Mater.* 10, 429–433. doi:10.1038/nmat3012.
- Collin, D., Lavallo, P., Garza, J. M., Voegel, J. C., Schaaf, P., and Martinoty, P. (2004). Mechanical properties of cross-linked hyaluronic acid/poly-(L-lysine) multilayer films. *Macromolecules* 37, 10195–10198. doi:10.1021/ma048683g.
- Cuevas, F. G., Montes, J. M., Cintas, J., and Urban, P. (2009). Electrical conductivity and porosity relationship in metal foams. *J. Porous Mater.* 16, 675–681. doi:10.1007/s10934-008-9248-1.
- Danine, A., Schoenleber, J., Ghanbaja, J., Montaigne, F., Boulanger, C., and Stein, N. (2018). Microstructure and thermoelectric properties of p-type bismuth antimony telluride nanowires synthesized by template electrodeposition in polycarbonate membranes. *Electrochim. Acta* 279, 258–268. doi:10.1016/j.electacta.2018.05.071.
- Deville, S. (2017). *Freezing Colloids : Observations, Principles, Control, and Use*. 1st ed. Springer, Cham.
- Dharmasena, K. P., and Wadley, H. N. G. (2002). Electrical conductivity of open-cell metal foams. *J. Mater. Res.* 17, 625–631. doi:10.1557/JMR.2002.0089.
- Dongmin Kang, S., and Jeffrey Snyder, G. (2017). Charge-transport model for conducting polymers. *Nat. Mater.* 16, 252–257. doi:10.1038/nmat4784.
- Dubochet J, Adrian M, Chang JJ, Homo JC, Lepault J, McDowell AW, Schultz P. (1988) Cryo-electron microscopy of vitrified specimens. *Q Rev Biophys.* 21, 129-228. doi:

10.1017/s0033583500004297.

- Efthymiou, C., Williams, M.A.K., McGrath, K.M. (2017) Revealing the structure of high-water content biopolymer networks: Diminishing freezing artefacts in cryo-SEM images, *Food Hydrocolloids*, 73, 203-212, doi.org/10.1016/j.foodhyd.2017.06.040.
- Feig, V. R., Tran, H., Lee, M., and Bao, Z. (2018). Mechanically tunable conductive interpenetrating network hydrogels that mimic the elastic moduli of biological tissue. *Nat. Commun.* 9, 1–9. doi:10.1038/s41467-018-05222-4.
- Finn, P. A., Asker, C., Wan, K., Bilotti, E., Fenwick, O., and Nielsen, C. B. (2021). Thermoelectric Materials: Current Status and Future Challenges. *Front. Electron. Mater.* 1, 1. doi:10.3389/femat.2021.677845.
- Frantz, C., Stein, N., Gravier, L., Granville, S., and Boulanger, C. (2010). Electrodeposition and characterization of bismuth telluride nanowires. *J. Electron. Mater.* 39, 2043–2048. doi:10.1007/s11664-009-1001-2.
- Goodall, R., Weber, L., and Mortensen, A. (2006). The electrical conductivity of microcellular metals. *J. Appl. Phys.* 100, 44912. doi:10.1063/1.2335672.
- Gordon, M. P., Zaia, E. W., Zhou, P., Russ, B., Coates, N. E., Sahu, A., et al. (2017). Soft PEDOT:PSS aerogel architectures for thermoelectric applications. *J. Appl. Polym. Sci.* 134, 44070. doi:10.1002/app.44456.
- Hamidi-Sakr, A., Biniek, L., Bantignies, J. L., Maurin, D., Herrmann, L., Leclerc, N., et al. (2017). A Versatile Method to Fabricate Highly In-Plane Aligned Conducting Polymer Films with Anisotropic Charge Transport and Thermoelectric Properties: The Key Role of Alkyl Side Chain Layers on the Doping Mechanism. *Adv. Funct. Mater.* 27, 1700173. doi:10.1002/ADFM.201700173.
- He, Y. (2005). Rapid thermal conductivity measurement with a hot disk sensor: Part 1. Theoretical considerations. *Thermochim. Acta* 436, 122–129. doi:10.1016/j.tca.2005.06.026.
- Hosseini, E., Ozhukil Kollath, V., and Karan, K. (2020). The key mechanism of conductivity in PEDOT:PSS thin films exposed by anomalous conduction behaviour upon solvent-doping and sulfuric acid post-treatment. *J. Mater. Chem. C* 8, 3982–3990. doi:10.1039/c9tc06311k.
- Hüsing, N., and Schubert, U. (1998). Aerogels - Airy Materials: Chemistry, Structure, and Properties. *Angew. Chemie - Int. Ed.* 37, 22–45. doi:10.1002/(sici)1521-3773(19980202)37:1/2<22::aid-anie22>3.0.co;2-i.
- Khan, Z. U., Edberg, J., Hamed, M. M., Gabrielsson, R., Granberg, H., Wågberg, L., Engquist, I., Berggren, M. and Crispin, X. (2016). Thermoelectric Polymers and their Elastic Aerogels. *Adv. Mater.* 28, 4556-4562. doi.org/10.1002/adma.201505364.
- Kim, G. H., Shao, L., Zhang, K., and Pipe, K. P. (2013). Engineered doping of organic semiconductors for enhanced thermoelectric efficiency. *Nat. Mater.* 12, 719–723. doi:10.1038/nmat3635.
- Kim, N., Lee, B. H., Choi, D., Kim, G., Kim, H., Kim, J. R., et al. (2012). Role of interchain coupling in the metallic state of conducting polymers. *Phys. Rev. Lett.* 109. doi:10.1103/PhysRevLett.109.106405.
- Kline, S. R., (2006) Reduction and analysis of SANS and USANS data using IGOR Pro *Journal of Applied Crystallography*, 39, 895–900. doi.org/10.1107/S0021889806035059

- Kroon, R., Ryan, J. D., Kiefer, D., Yu, L., Hynynen, J., Olsson, E., et al. (2017). Bulk Doping of Millimeter-Thick Conjugated Polymer Foams for Plastic Thermoelectrics. *Adv. Funct. Mater.* 27, 1704183. doi:10.1002/adfm.201704183.
- Liu, P. S., Li, T. F., and Fu, C. (1999). Relationship between electrical resistivity and porosity for porous metals. *Mater. Sci. Eng. A* 268, 208–215. doi:10.1016/s0921-5093(99)00073-8.
- Maeda, R., Kawakami, H., Shinohara, Y., Kanazawa, I., and Mitsuishi, M. (2019). Thermoelectric properties of PEDOT/PSS films prepared by a Gel-film formation process. *Mater. Lett.* 251, 169–171. doi:10.1016/j.matlet.2019.05.005.
- Maeda, R., Shinohara, Y., Kawakami, H., Isoda, Y., Kanazawa, I., and Mitsuishi, M. (2020). The Conducting Fibrillar Networks of a PEDOT:PSS Hydrogel and an Organogel Prepared by the Gel-film Formation Process. *Nanotechnology* 32, 135403. doi:10.1088/1361-6528/abd1a9.
- Massonnet, N., Carella, A., De Geyer, A., Faure-Vincent, J., and Simonato, J. P. (2014). Metallic behaviour of acid doped highly conductive polymers. *Chem. Sci.* 6, 412–417. doi:10.1039/C4SC02463J.
- Noroozi, M., Panahi-Sarmad, M., Abrisham, M., Amirikiai, A., Asghari, N., Golbaten-Mofrad, H., et al. (2019). Nanostructure of Aerogels and Their Applications in Thermal Energy Insulation. *ACS Appl. Energy Mater.* 2, 5319–5349. doi:10.1021/acsaem.9b01157.
- Rouquerol, J., Llewellyn, P., Rouquerol, F. (2007), Is the BET Equation Applicable to Microporous Adsorbents?, *Studies in Surface Science and Catalysis*, 160, 49-56, doi: 10.1016/S0167-2991(07)80008-5
- Rubinstein, M., and Colby, R. H. (2003). *Thermodynamics of Mixing*. Oxford: Oxford university press.
- Scheunemann, D., and Kemerink, M. (2020). Non-Wiedemann-Franz behavior of the thermal conductivity of organic semiconductors. *Phys. Rev. B* 101, 75206. doi:10.1103/PhysRevB.101.075206.
- Slack, G. A. (1995). “New materials and performance limits for thermoelectric cooling,” in *CRC Handbook of Thermoelectrics*, ed. D. M. Rowe (CRC Press), 399–432.
- Sommerfeld, A. (1927). Zur Elektronentheorie der Metalle. *Naturwissenschaften* 15, 825–832. doi:10.1007/BF01505083.
- Takano, T., Masunaga, H., Fujiwara, A., Okuzaki, H., and Sasaki, T. (2012). PEDOT nanocrystal in highly conductive PEDOT:PSS polymer films. *Macromolecules* 45, 3859–3865. doi:10.1021/ma300120g.
- Tang, G. H., Bi, C., Zhao, Y., and Tao, W. Q. (2015). Thermal transport in nano-porous insulation of aerogel: Factors, models and outlook. *Energy* 90, 701–721. doi:10.1016/j.energy.2015.07.109.
- Topsøe, H. (1968). Geometric factors in four point resistivity measurement. *Bridg. Technol.*
- Vijayakumar, V., Zhong, Y., Untilova, V., Bahri, M., Herrmann, L., Biniek, L., et al. (2019). Bringing Conducting Polymers to High Order: Toward Conductivities beyond 10^5 S cm^{-1} and Thermoelectric Power Factors of $2 \text{ mW m}^{-1} \text{ K}^{-2}$. *Adv. Energy Mater.* 9, 1–12. doi:10.1002/aenm.201900266.
- Walton, K. S., Snurr, R. Q., (2007), Applicability of the BET Method for Determining Surface Areas of Microporous Metal-Organic Frameworks, *Journal of the American Chemical Society*, 129, 27,

8552-8556, doi: 10.1021/ja071174k.

- Wang, X., Liu, P., Jiang, Q., Zhou, W., Xu, J., Liu, J., et al. (2019). Efficient DMSO-Vapor Annealing for Enhancing Thermoelectric Performance of PEDOT:PSS-Based Aerogel. *ACS Appl. Mater. Interfaces* 11, 2408–2417. doi:10.1021/acsami.8b19168.
- Weinbach, Q., Nielsen, C. B., and Biniek, L. (2021). Multi length scale porosity as a playground for organic thermoelectric applications. *J. Mater. Chem. C* 9, 10173–10192. doi:10.1039/d1tc02331d.
- Woignier, T., Phalippou, J., Despetis, F., and Calas-Etienne, S. (2018). “Aerogel Processing,” in *Handbook of Sol-Gel Science and Technology: Processing, Characterization and Applications*, eds. L. Klein, M. Aparicio, and A. Jitianu (Springer, Cham), 985–1011. doi:10.1007/978-3-319-32101-1_27.
- Yanagishima, N., Kanehashi, S., Saito, H., Ogino, K., and Shimomura, T. (2020). Thermoelectric properties of PEDOT:PSS aerogel secondary-doped in supercritical CO₂ atmosphere with low thermal conductivity. *Polymer* 206, 122912. doi:10.1016/j.polymer.2020.122912.
- Yao, B., Wang, H., Zhou, Q., Wu, M., Zhang, M., Li, C., et al. (2017). Ultrahigh-Conductivity Polymer Hydrogels with Arbitrary Structures. *Adv. Mater.* 29, 1700974. doi:10.1002/adma.201700974.
- Zhang, X., Chang, D., Liu, J., and Luo, Y. (2010). Conducting polymer aerogels from supercritical CO₂ drying PEDOT-PSS hydrogels. *J. Mater. Chem.* 20, 5080–5085. doi:10.1039/c0jm00050g.

SUPPORTING INFORMATION

Efficient control of a mesoporous fibrillar PEDOT:PSS aerogel structure for promising thermoelectric applications

Quentin Weinbach,¹ Swapneel Vijay Thakkar,¹ Alain Carvalho,¹ Gérald Chaplais,^{2,3} Jérôme Combet,¹ Doru Constantin,¹ Nicolas Stein,⁴ Dominique Collin,¹ Laure Biniek^{1*}

¹ Université de Strasbourg, CNRS, Institut Charles Sadron UPR22, F-67000 Strasbourg, France

² Université de Haute-Alsace, CNRS, Institut de Science des Matériaux de Mulhouse (IS2M), UMR 7361, F-68100 Mulhouse, France

³ Université de Strasbourg, 67000 Strasbourg, France

⁴ Université de Lorraine, CNRS, IJL, F-57000 Metz, France

*E-mail: laure.biniek@ics-cnrs.unistra.fr

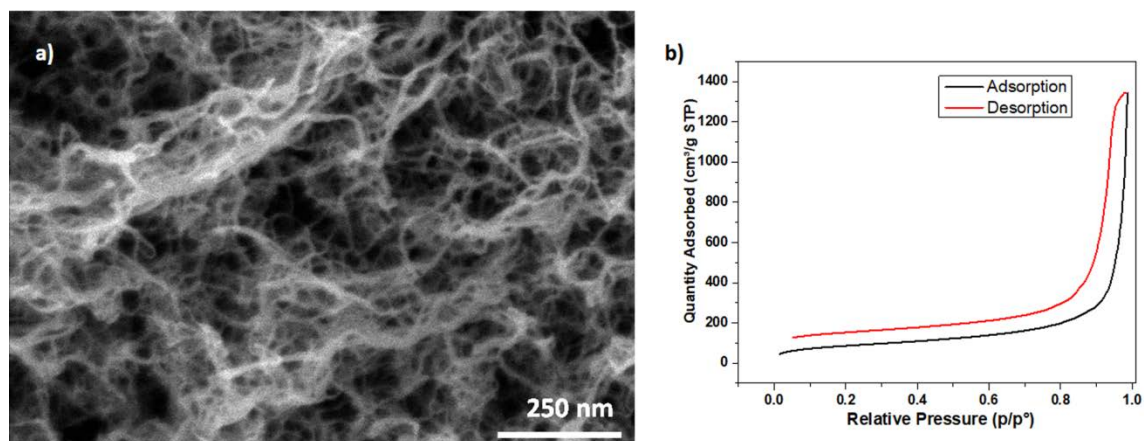


Figure ESI1: a) cryo-SEM image of the PEDOT:PSS aerogel at high magnification, b) Typical nitrogen adsorption and desorption isotherms.

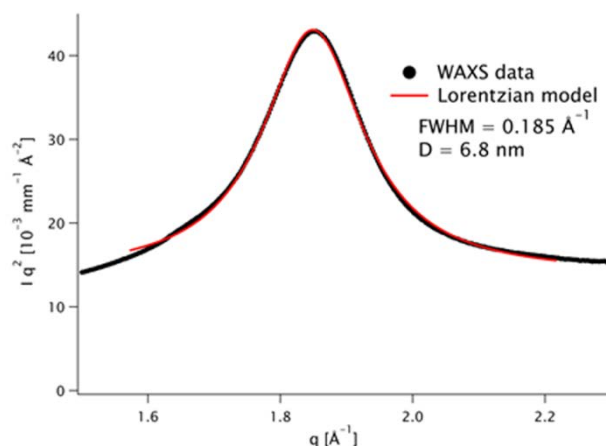


Figure ESI2: Kratky plot ($I q^2$ vs. q) of the WAXS data in Figure 2d (solid dots) and Lorentzian fit of the 3.4 Å peak (solid line).

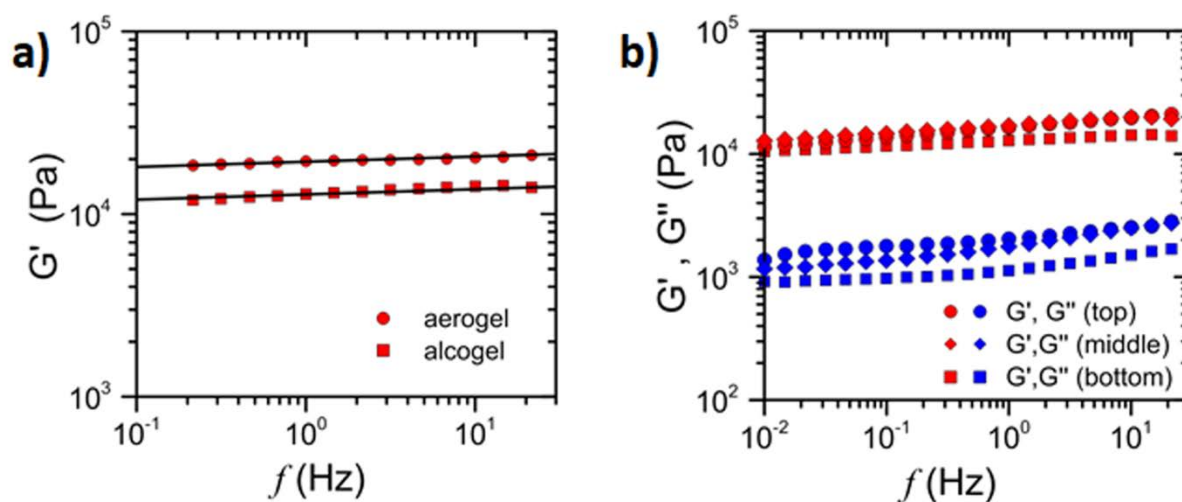


Figure ESI 3: a) Elastic moduli variation with the frequency for the alcogel and the aerogel. This variation can be well fitted, in first approximation, by linear relationship with the same slope. Using this approximation, the ratio of the elastic moduli of the alcogel over the ones of the aerogel can be determined and thus compared with the change in volume induced by supercritical drying. b) Shear measurements for three slices cut in the same alcogel sample (top, middle and bottom part of ~ 1.5 mm thickness each). The results obtained show no significant variation of the G' - and G'' -values with the alcogel slice. These results are in agreement with a homogeneous description of the sample at a macroscopic level.

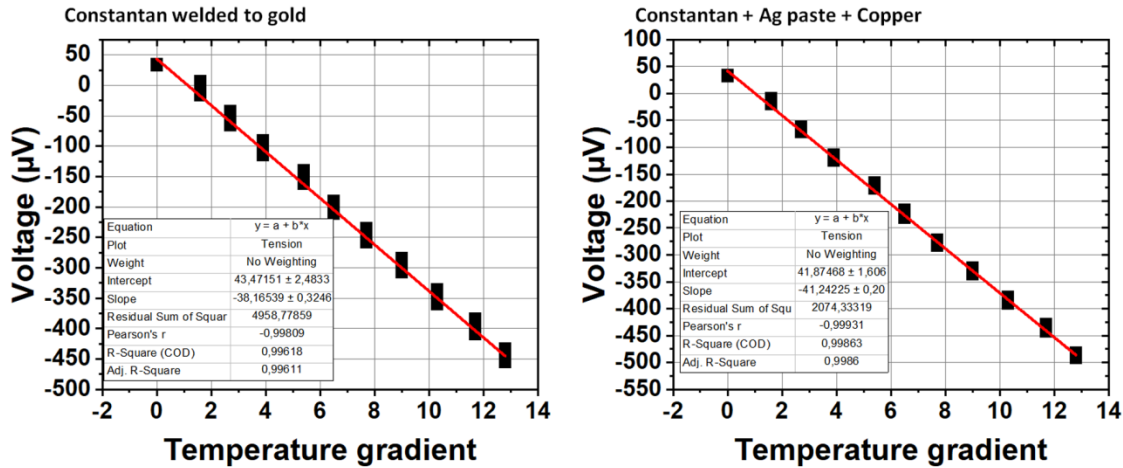


Figure ES14: In-plane Seebeck coefficient measurement. To ensure a good electrical contact with the probes and a good thermal contact with the Peltier elements, aerogels samples have been pasted on copper foil (Cu) with silver paste (Ag). The use of copper and silver paste has a slight impact on the open voltage measured. This has been confirmed by comparing the measurements for a reference constantan wire (welded to gold with tin or contacted with silver paste on top of copper foil). The Seebeck coefficient measured on the set-up using Cu-Ag is $3 \mu\text{V/K}$ lower (i.e. $-41.2 \mu\text{V/K}$) as compared to the reference value of $-38.1 \mu\text{V/K}$ for constantan at room temperature. Therefore, in this work, all in-plane Seebeck coefficient values were corrected by addition of $3 \mu\text{V/K}$.

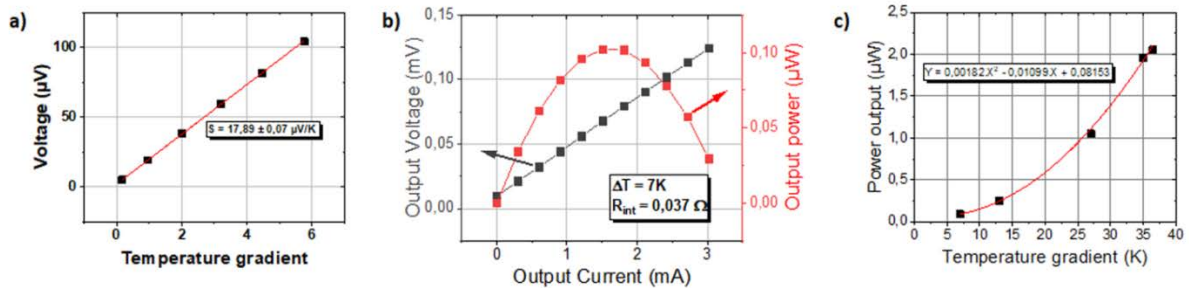


Figure ES15: a) Cross-plane Seebeck coefficient measurement, thermovoltage at various temperature differences. b) Output voltage and output power as a function of current for a typical aerogel at a temperature gradient of 7K . c) Evolution of the power output as a function of the temperature gradient fitted with a 2nd order polynomial function.

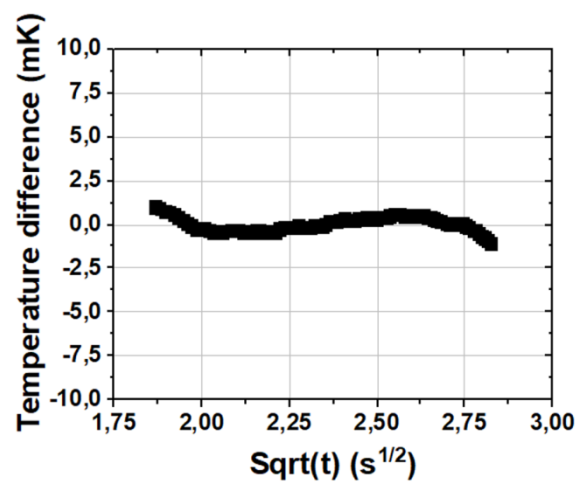


Figure ESI6: Typical residual curve obtained while measuring the thermal conductivity of PEDOT:PSS aerogel.